FIRST SURVEY OF FINITE-BETA MAGNETIC FIELDS OF W7-X

E. Strumberger

IPP 2/339 **December 1997**

MAX-PLANCK-INSTITUT FÜR PLASMAPHYSIK

D-85748 Garching bei München, Germany

Die nachstehende Arbeit wurde im Rahmen des Vertrages zwischen dem Max-Planck-Institut für Plasmaphysik und der Europäischen Atomgemeinschaft über die Zusammenarbeit auf dem Gebiet der Plasmaphysik durchgeführt

Table of contents

Abstract

Magnetic fields are calculated for finite-β equilibria of up to $\langle\beta\rangle = 5\%$ and rotational transform values of $\iota = 5/5,\ 5/6,\ 5/4$ (rotational transform in the edge region) in W7-X. For these computations a system of numerical codes is used that allows to calculate vacuum magnetic fields and to trace field lines (GOURDON code), to compute fixed-boundary (VMEC code) and free-boundary equilibria (NEMEC code), to determine the magnetic fields of these equilibria (MFBE code) and to analyse their magnetic field and MHD stability properties (JMC code). Comparisons of the finite-β magnetic fields with the corresponding vacuum fields yield informations about the shift of the plasma column, variations of the apect ratio, the ι-profil, the magnetic mirror, the widths of the macroscopic islands and the ergodization of the edge region with increasing β. Furthermore, the dependencies of these properties on the mass profile that is assumed in the NEMEC code are investigated.

1.0 Introduction

The optimized Wendelstein 7-X (W7-X) Helias stellarator [1, 2] is expected to reach volume averaged β-values of up to 5%. Part of the experimental flexibility will be achieved by modifying the rotational transform in the range $5/6 \leq \iota \leq 5/4$. In order to optimize the divertor geometry [3 – 5] for various plasma equilibria and to improve SOL studies [6 – 8], detailed knowledge of the corresponding magnetic field structures is necessary. For this purpose, magnetic fields are calculated for finite-β equilibria of up to $\langle\beta\rangle = 5\%$ and edge rotational transform values of $\iota = 5/5,\ 5/6,\ 5/4$.

For these first computations the following system of numerical codes is used. The GOURDON code calculates the vacuum magnetic field, traces field lines and computes the rotational transform and the magnetic well. Further, the last closed magnetic surface (LCMS) is determined. It lies inside the macroscopic islands (5/6, 5/5 or 5/4 islands) because these islands are intersected by divertor plates [3, 4, 8]. The data of the coordinates along the field line forming the LCMS are used in the DESCUR code [9] to approximate the LCMS by a set of Fourier coefficients. These coefficients serve as plasma boundary description for the fixed-boundary VMEC code (**V**ariational **M**oments **E**quilibrium **C**ode) [10, 11], which assumes nested magnetic surfaces, and as initial guess of this boundary for the three-dimensional free-boundary equilibrium NEMEC code [11]. The NEMEC code is a synthesis of the VMEC code and the NESTOR (**NE**umann **S**olver for **TO**roidal **R**egions) vacuum code [12]. It computes free-boundary finite-β Helias equilibria. Using the results obtained with the NEMEC code the MFBE code (**M**agnetic Field Solver for **F**inite-**B**eta **E**quilibria) [13] calculates the magnetic field of the finite-β equilibrium on a grid inside and outside the plasma boundary. This magnetic field serves as input to the GOURDON code, which is used to determine the LCMS of the finite-β equilibrium. If this LCMS does not coincide with the plasma boundary obtained by the NEMEC code, the toroidal flux, which is a free parameter in the NEMEC code, is modified, that is, the toroidal flux is determined iteratively [13]. Finally, the JMC code [14 – 16] yields the Fourier spectrum of the magnetic field and investigates the stability of the three-dimensional finite-β equilibrium with respect to Mercier [17] and resistive interchange modes [18].

This report is organized as follows. In Section 2 vacuum magnetic fields with edge rotational transform values of $\iota = 5/5,\ 5/6,\ 5/4$ (Section 2.1), and their properties (e.g. ι-profile, magnetic well, magnetic mirror) (Section 2.2) are discussed. The corresponding finite-β equilibria with volume averaged β-values of up to 5% are treated in Section 3. There, the finite-β magnetic field properties are studied (Section 3.1) and the MHD stability properties are investigated (Section 3.2). Furthermore, the dependencies of the finite-β results on the mass profile that is assumed in the NEMEC code are studied in Section 3.3. Finally, in Section 4 a short summary of the results is given.

2. Vacuum magnetic fields

2.1 Coil currents

The actual coil system HS5V10U of W7-X consists of fifty modular non-planar coils and twenty auxiliary planar, non-circular coils, that is, ten modular and four auxiliary coils for each of the five periods. The coils are superconducting and produce a magnetic field strength of 2.5 T on the magnetic axis. Because of the periodicity and the stellarator symmetry only the five modular and the two auxiliary coil currents of half a period are free for variations, while the other currents are determined by the symmetry conditions of stellarator symmetry. That is, there are seven degrees of freedom to produce various magnetic fields.

For the three magnetic field configurations considered in this work the coil currents given in Table I have been chosen.

TABLE I: Currents of the modular coils 1-5 and the planar coils $\mathcal{A}$ and $\mathcal{B}$ for three magnetic field configurations of W7-X. I_n [MA] is the nominal coil current for producing a magnetic field strength of $\langle B_0 \rangle = 2.5$ T averaged along the magnetic axis. F_c is the factor related to the cases A, B and C for each coil type given in the Table leading to an individual coil current $I_c = I_n F_c$.

	I_n	F_c						
	[MA]	1	2	3	4	5	$\mathcal{A}$	$\mathcal{B}$
A	1.32	1.0	1.0	1.0	1.0	1.0	0.245	0.245
B	1.45	1.0	1.0	1.0	1.0	1.0	0.000	0.000
C	1.60	1.0	1.0	1.0	1.0	1.0	-0.230	-0.230

Case A is the so-called low-iota case ($\iota = 5/6$ in the edge region), that is, a chain of six islands surrounds the LCMS. This low rotational transform is realized by equal modular coil currents and currents through the auxiliary coils in the same direction as those in the modular coils. Case B is characterized by five islands ($\iota = 5/5$) outside the last closed magnetic surface. It is called standard case and is realized by equal modular coil currents and no auxiliary coil currents. In order to obtain the high-iota case C ($\iota = 5/4$ in the edge region), negative currents through the auxiliary coils are added. Case C is characterized by four remnants of islands embedded in a stochastic edge region.

2.2 Properties of the vacuum magnetic fields

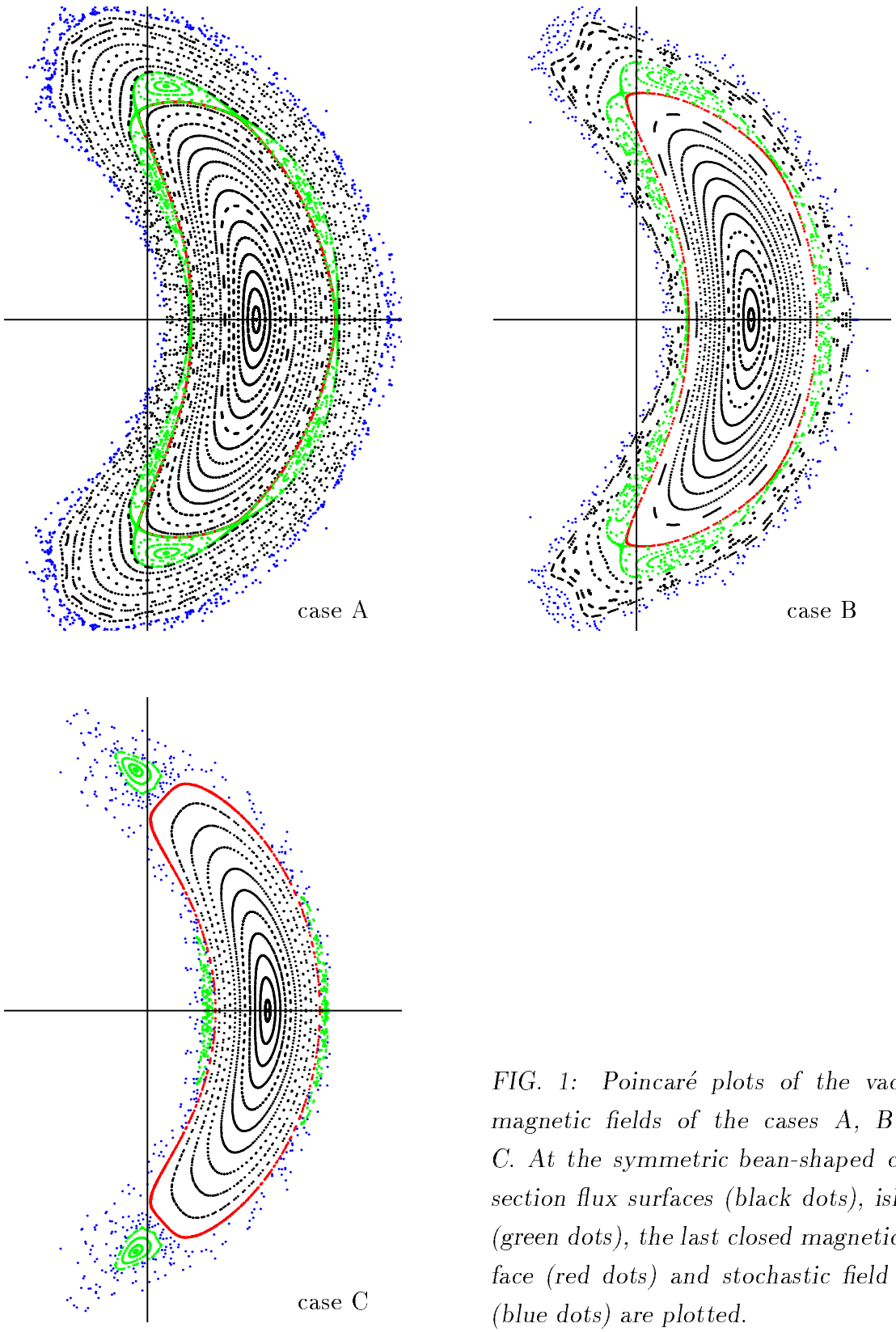

FIG. 1: Poincaré plots of the vacuum magnetic fields of the cases A, B and C. At the symmetric bean-shaped cross-section flux surfaces (black dots), islands (green dots), the last closed magnetic surface (red dots) and stochastic field lines (blue dots) are plotted.

The vacuum magnetic field configurations of the cases A, B and C are shown in Fig. 1. For the cases A and B the macroscopic islands (5/6 and 5/5 islands) are surrounded by closed magnetic surfaces lying further out, while for case C the region of closed magnetic surfaces is reduced. Here only remnants of four islands embedded in a stochastic edge region are found.

The largest Fourier coefficients of the vacuum magnetic fields in magnetic coordinates [16, 19] versus $\sqrt{s}$ (s = flux label) are plotted in Fig. 2. There, the component $B_{0,0}$ describes the main magnetic field (containing the deepening of the magnetic well at finite β), $B_{1,1}$ represents the helical curvature, $B_{1,0}$ the toroidal curvature and $B_{0,1}$ the mirror field.

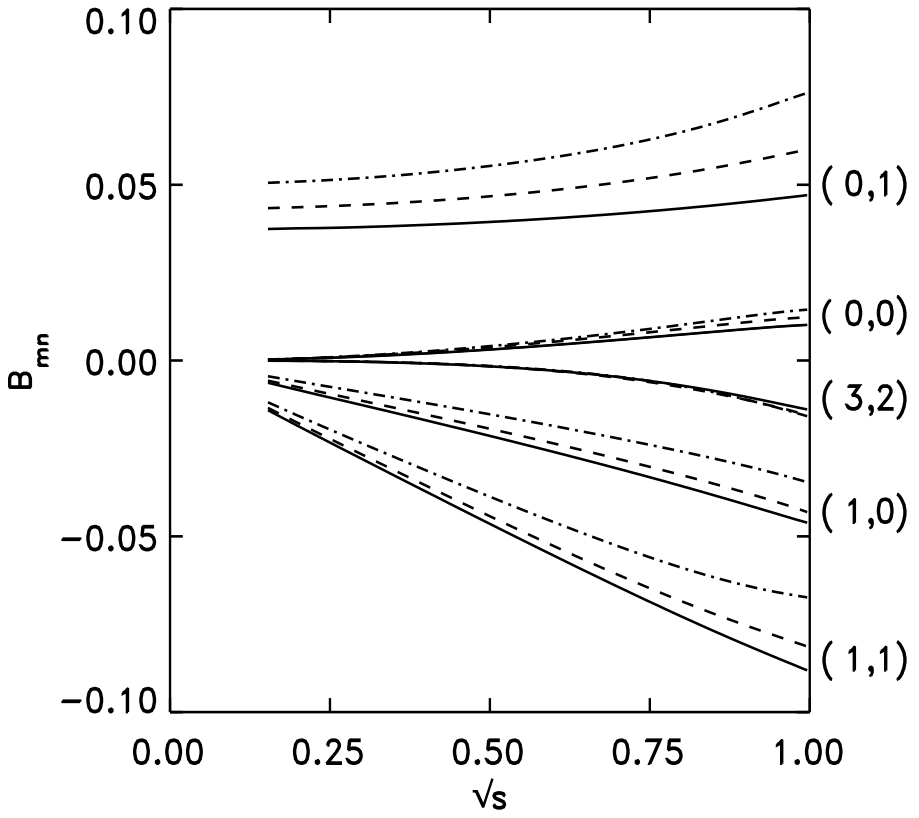

FIG. 2: The $B_{\mathrm{m,n}}$s for the cases A (solid line), B (dashed line) and C (dashed dotted line) are plotted versus $\sqrt{s}$ with s = flux label. Fourier coefficients smaller than 0.01 are not shown. $B_{0,0}(s=0)=1$ has been subtracted in plotting $B_{0,0}$.

The Fourier coefficient $B_{0,1}$ corresponds to a mirror field of approximately 4% for the low-iota case (case A), of 5% for the standard case (case B) and of approximately 6% for the high-iota case (case C).

The profiles of the rotational transform ι and the magnetic well V'' are plotted for the cases A, B and C in Figs 3 and 4.

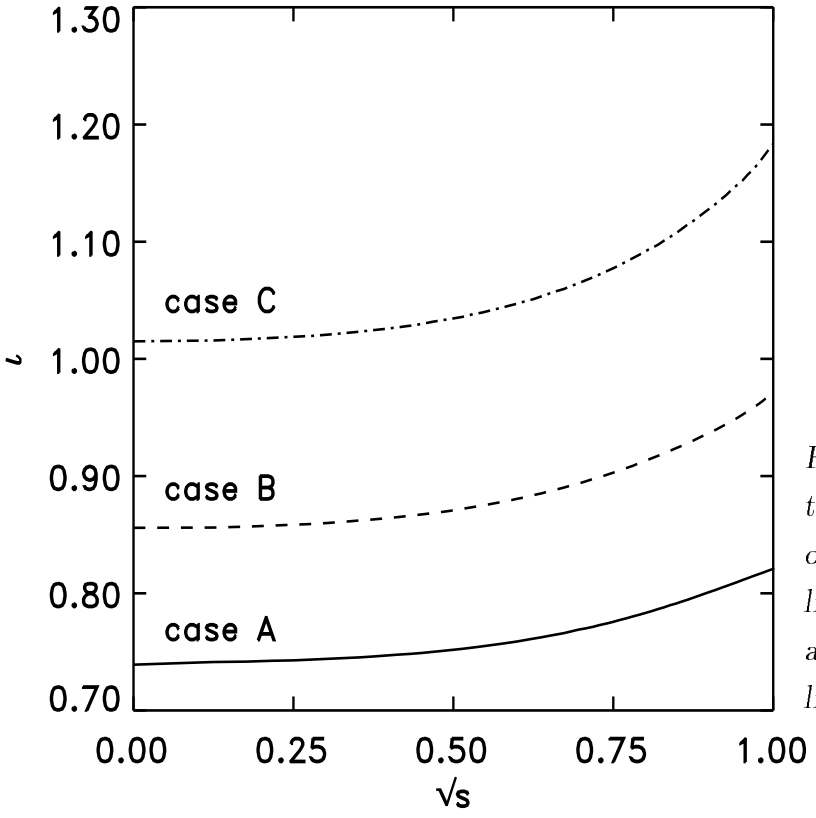

FIG. 3: Rotational transform profiles ι of the cases A (solid line), B (dashed line) and C (dashed dotted line).

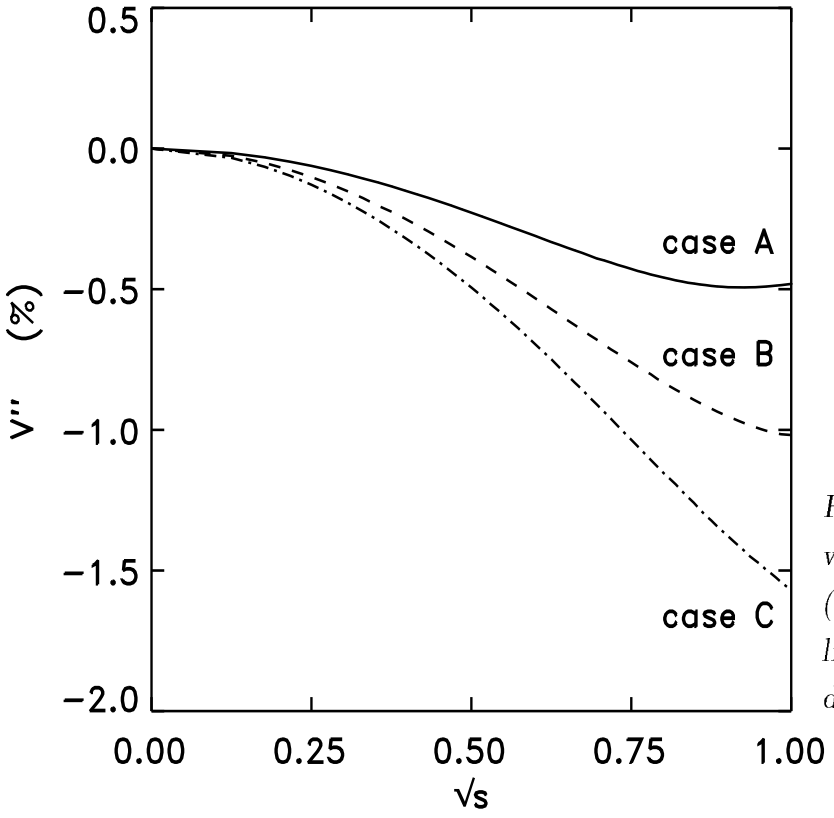

FIG. 4: Magnetic wells V'' of the cases A (solid line), B (dashed line) and C (dashed dotted line).

The vacuum magnetic field properties of the cases A, B and C are summed up in Table II, which contains the rotational transform ι_0 on the magnetic axis, the aspect ratio A, the magnetic well V'' and the volume V inside the LCMS. The comparison of the three cases shows that the aspect ratio and the magnetic well increase with increasing rotational transform, while the volume inside the LCMS decreases.

TABLE II: Rotational transform ι_0 on the magnetic axis, aspect ratio A, magnetic well $V'' = (V'_{LCMS} - V'_0)/V'_0$ (V'_{LCMS} = specific volume on the LCMS, V'_0 = specific volume on the magnetic axis) and volume V enclosed by the LCMS for the vacuum magnetic field configurations A, B and C.

case	ι_0	A	V'' [%]	V [m^3]
A	0.739	10.5	-0.48	29.8
B	0.856	10.6	-1.02	29.4
C	1.015	11.5	-1.57	24.9

3. Finite-β equilibria

Magnetic fields are calculated for finite-β equilibria of up to $\langle\beta\rangle = 5\%$ for the cases A, B and C. For this purpose, free-boundary equilibria are computed by means of the NEMEC code [11]. There, the adiabatic conservation of the mass between neighbouring flux surfaces requires for the pressure profile $p(s)$ [20]

$$p(s) = m(s)(V'(s))^{-\gamma},$$

with s = radial coordinate labeling a magnetic flux surface, $V'(s)$ = differential volume element, m(s) = mass profile, which has to be provided as input, and $\gamma \geq 0$ being the adiabatic index. Here $\gamma = 2$ and two types of mass profile m, shown in Fig. 5, are used.

Type I : $m(s) = a_0(1 - 2s + s^2)$

Type II: $m(s) = a_1(1 - \frac{11}{7}s + \frac{4}{7}s^2)$

The constants a_0 and a_1 depend on the desired β-value. In order to obtain the same $\langle\beta\rangle$ for the two profiles $a_1/a_0 \approx 0.82$ has to be fulfilled.

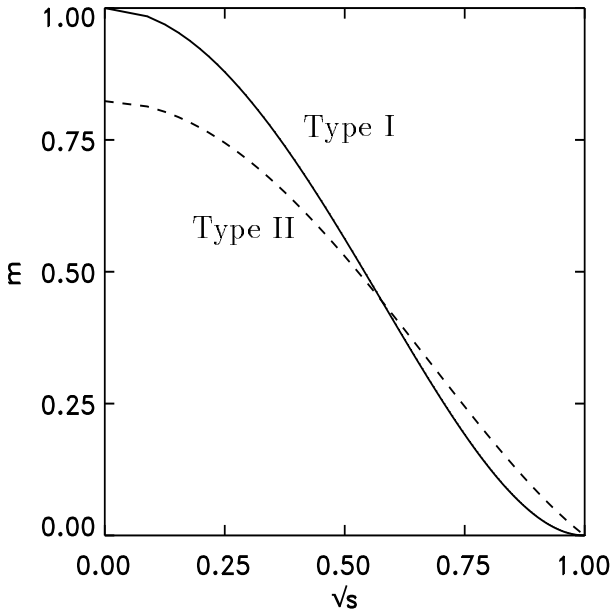

FIG. 5: Mass profiles m of Type I (solid line) and Type II (dashed line).

The mass profile Type I is used for the calculations presented in Section 3.1 and 3.2. For $\langle\beta\rangle = 4\%$ the computations are repeated using mass profile Type II. In Section 3.3 these results are compared with those obtained for profile Type I.

The magnetic fields of the finite-β equilibria are determined on a grid by using the MFBE code [13]. The combination of the NEMEC and MFBE code allows an iterative determination of the toroidal flux, so that the LCMS used in the NEMEC code is identical with the one obtained by field line tracing.

3.1 Finite-β magnetic field properties

Here the finite-β magnetic field properties of the low-iota, standard and high-iota cases (cases A, B and C) are discussed. Figures 6a and 6b show the Poincaré plots of the finite-β magnetic fields and their corresponding vacuum fields at the bean-shaped cross-section.

For the high-iota case (case C) finite-β equilibria could only be obtained up to $\langle\beta\rangle = 4\%$ in the framework of the used method (NEMEC + MFBE code), but $\langle\beta\rangle = 5\%$ may be reached by a more appropriate choice of the coil currents, that is, by an increase of the vertical field component B_z, which leads to an inward shift of the plasma column.

For $\langle\beta\rangle \geq 3\%$ the low-order resonances 5/7 (case A), 5/6 (case B) and 5/5 (case C) appear inside the last closed magnetic surfaces. In Figs 6a and 6b these islands are illustrated by pink dots. With increasing β these islands approach the LCMS.

The width of the macroscopic 5/5 islands (see Fig. 6b, case B, green dots) increases with increasing β, while the remnants of the macroscopic 5/4 islands (see Fig. 6b, case C, green dots) become smaller because of the increasing stochasticity of the edge region (blue dots) [21]. The positions of the X- and O-Points of these macroscopic islands are almost unchanged (see also Figs 7b and 7c). The width of the macroscopic 5/6 islands (see Fig. 6a, case A, green dots and Fig. 7a) decreases up to $\langle\beta\rangle = 3\%$. For $\langle\beta\rangle \geq 4\%$ phase shifts of these macroscopic islands and also of the 5/7 and 10/11 islands are observed. As shown in more detail in Fig. 8, the phase shifts of the 5/6 and 10/11 islands occur between $\langle\beta\rangle = 3\%$ and $\langle\beta\rangle = 4\%$, while the phase shift of the 5/7 islands takes place between $\langle\beta\rangle = 4\%$ and 5%. It will be interesting to compare these results with those obtained by other codes, e.g. the PIES code (**P**rincton **I**terative **E**quilibrium **S**olver) [22 – 24]. Here the islands inside the LCMS are not obtained in a self-consistent way since the VMEC code supposes the existence of nested magnetic surfaces.

FIGs 6a,b: Poincaré plots of the magnetic fields of the cases A, B and C for $0 \leq \langle\beta\rangle \leq 5\%$ (see pages 10 and 11). At the symmetric bean-shaped cross-section flux surfaces (black dots), macroscopic islands (green dots), the last closed magnetic surface (red dots) and stochastic field lines (blue dots) are plotted. For $\langle\beta\rangle \geq 3\%$ the rotational transform values 5/7 (case A), 5/6 (case B) and 5/5 (case C) appear (pink dots).

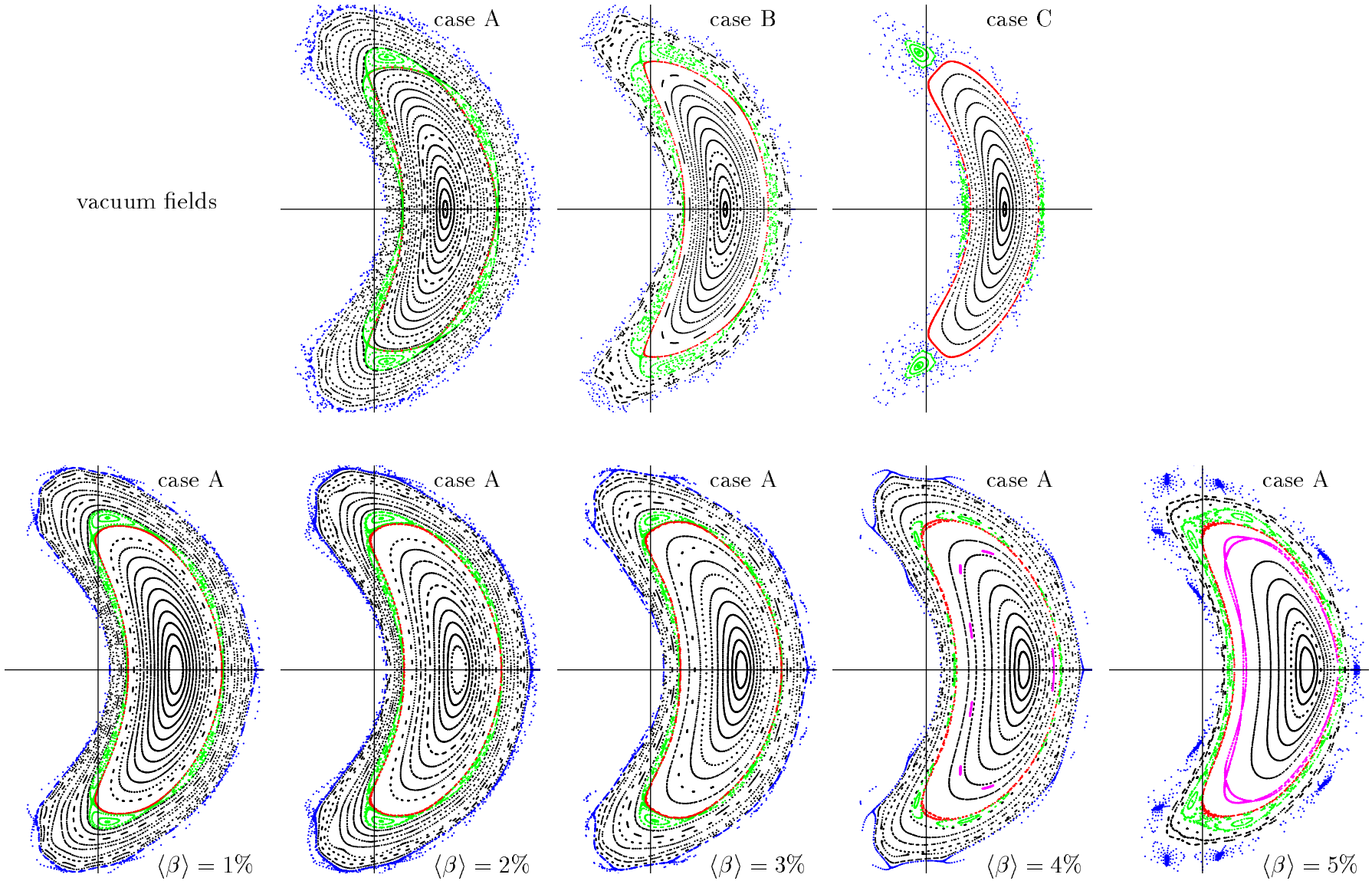
vacuum fields
case A
case B
case C
case A
case A
case A
case A
case A
$\langle\beta\rangle = 1\%$
$\langle\beta\rangle = 2\%$
$\langle\beta\rangle = 3\%$
$\langle\beta\rangle = 4\%$
$\langle\beta\rangle = 5\%$

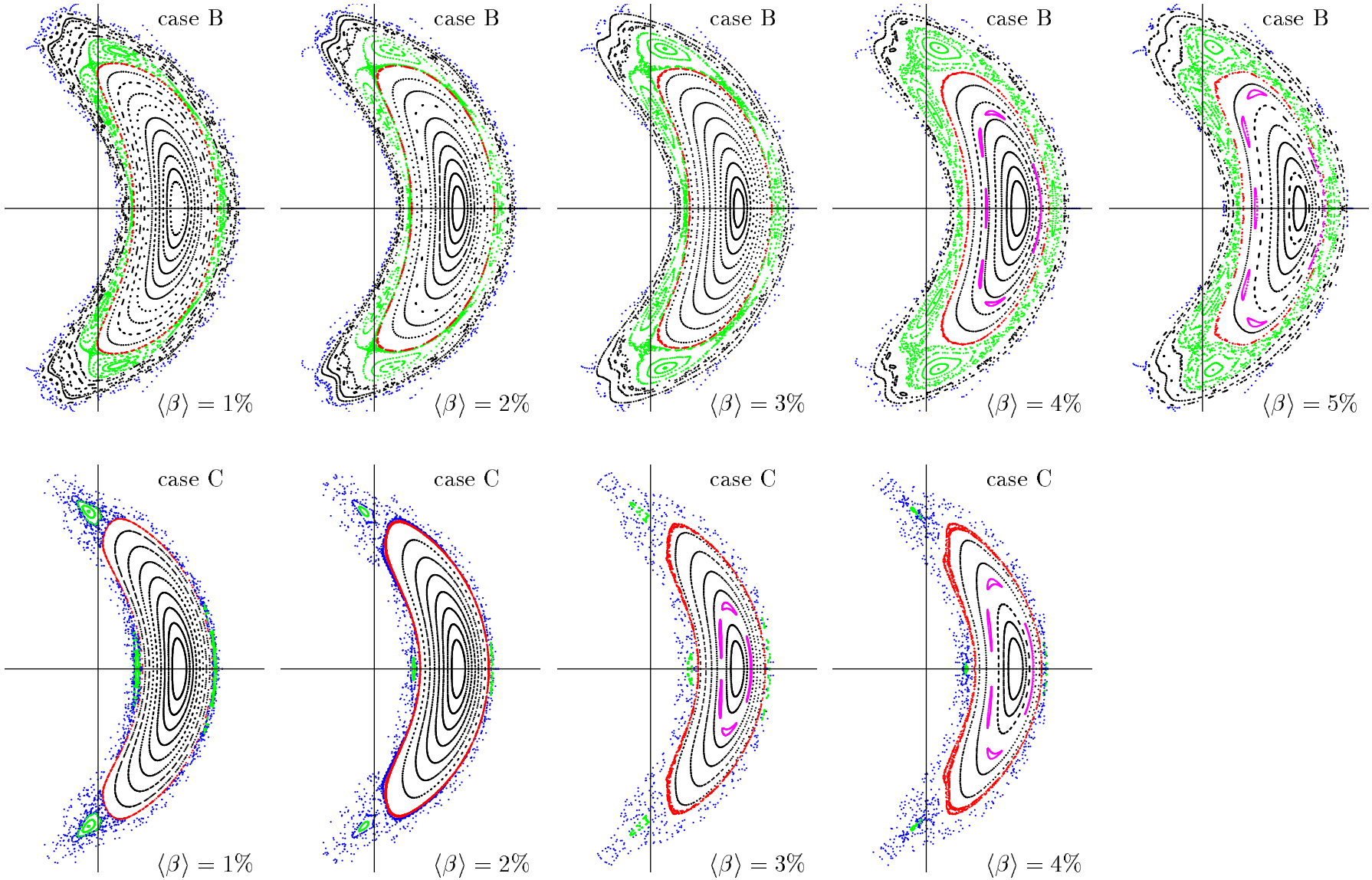
case B
$\langle\beta\rangle = 1\%$
case B
$\langle\beta\rangle = 2\%$
case B
$\langle\beta\rangle = 3\%$
case B
$\langle\beta\rangle = 4\%$
case B
$\langle\beta\rangle = 5\%$
case C
$\langle\beta\rangle = 1\%$
case C
$\langle\beta\rangle = 2\%$
case C
$\langle\beta\rangle = 3\%$
case C
$\langle\beta\rangle = 4\%$

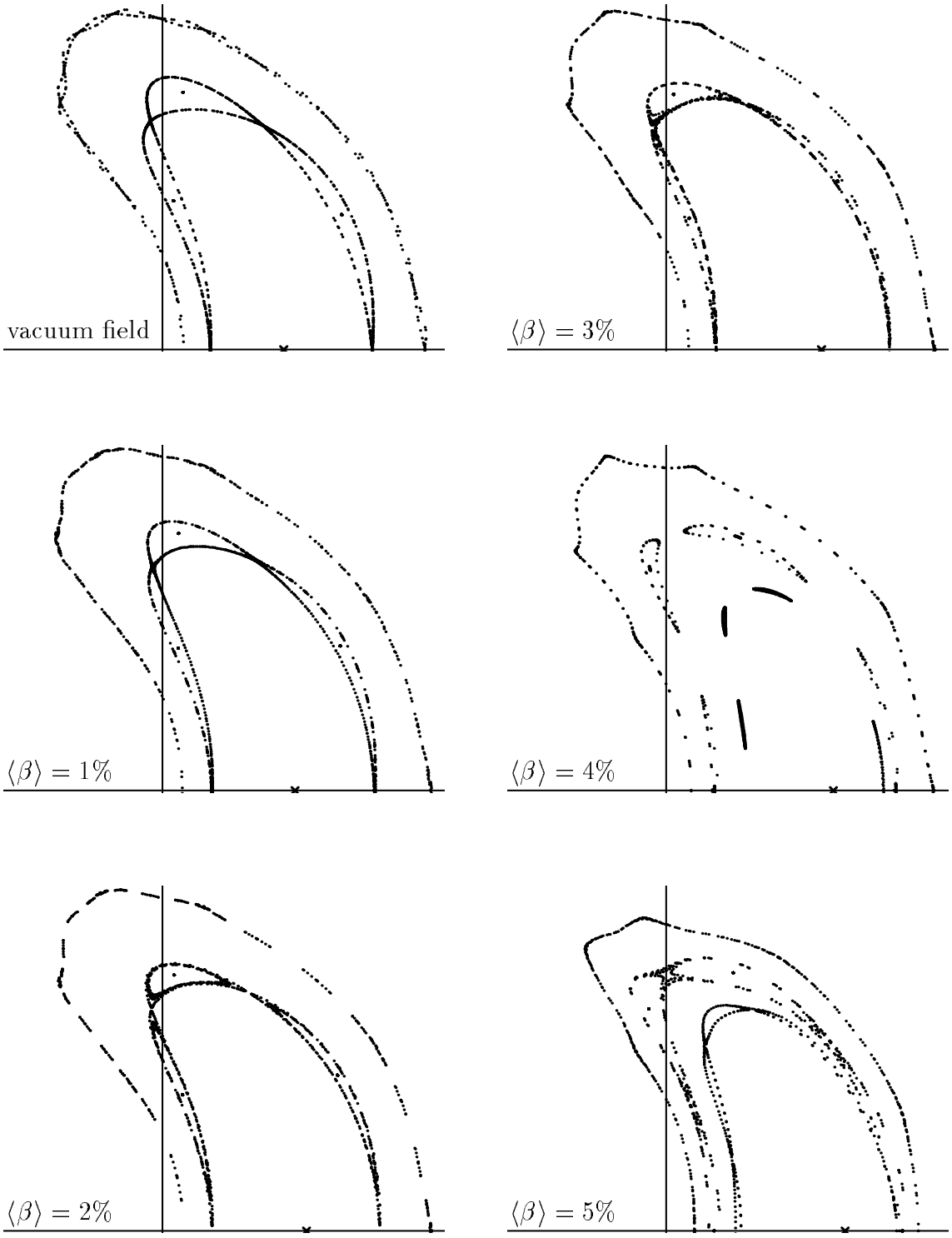

FIG. 7a: Upper halves of Poincaré plots of the low-iota case (case A) for various β-values. At the symmetric bean-shaped cross-section the magnetic axis (cross), the macroscopic islands with their O-points and the outermost closed magnetic flux surface are plotted. For $\langle\beta\rangle = 4$ and 5% also the 5/7 islands inside the plasma are shown.

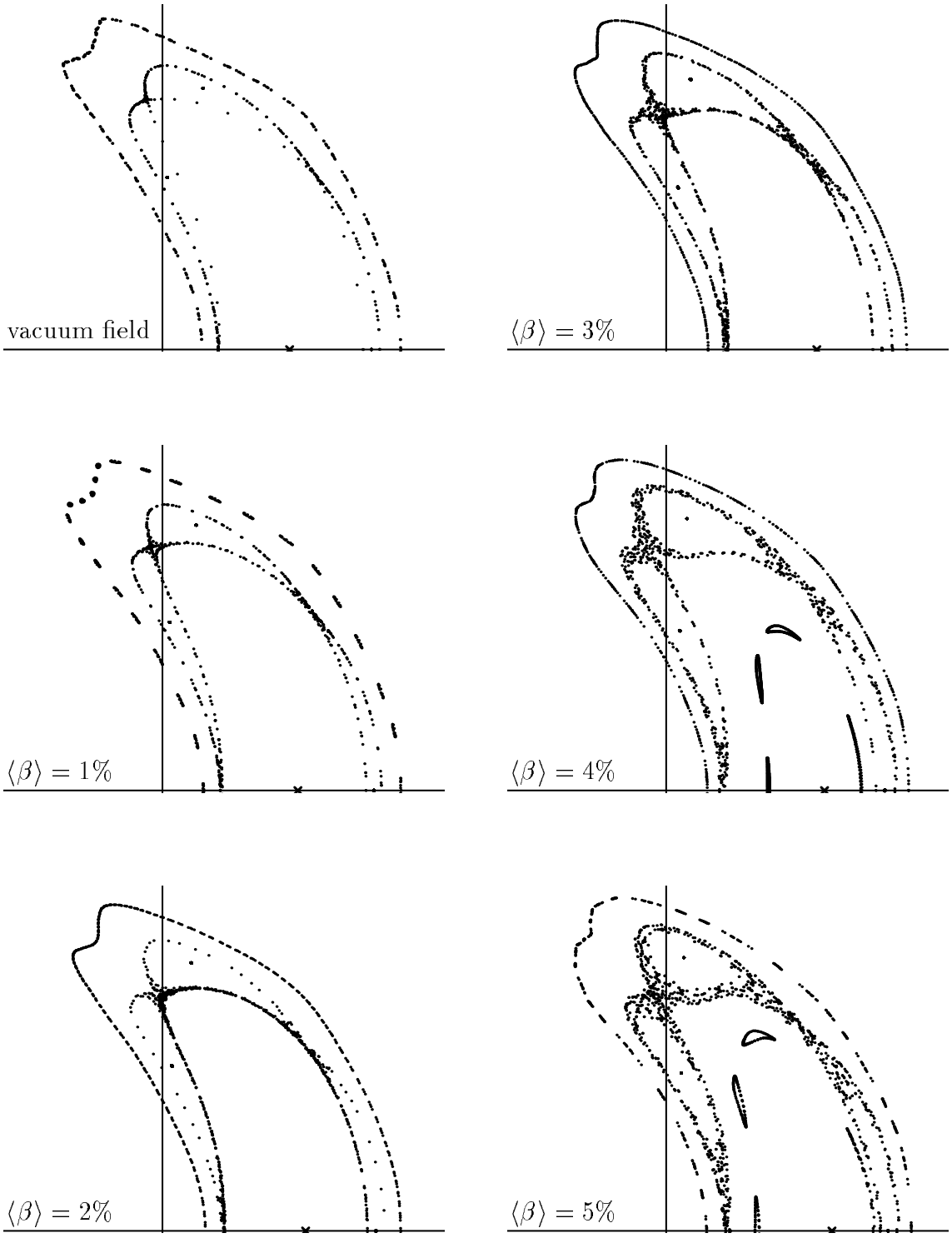

FIG. 7b: Upper halves of Poincaré plots of the standard case (case B) for various β-values. At the symmetric bean-shaped cross-section the magnetic axis (cross), the macroscopic islands with their O-points and the outermost closed magnetic flux surface are plotted. For $\langle\beta\rangle = 4$ and 5% also the 5/6 islands inside the plasma are shown.

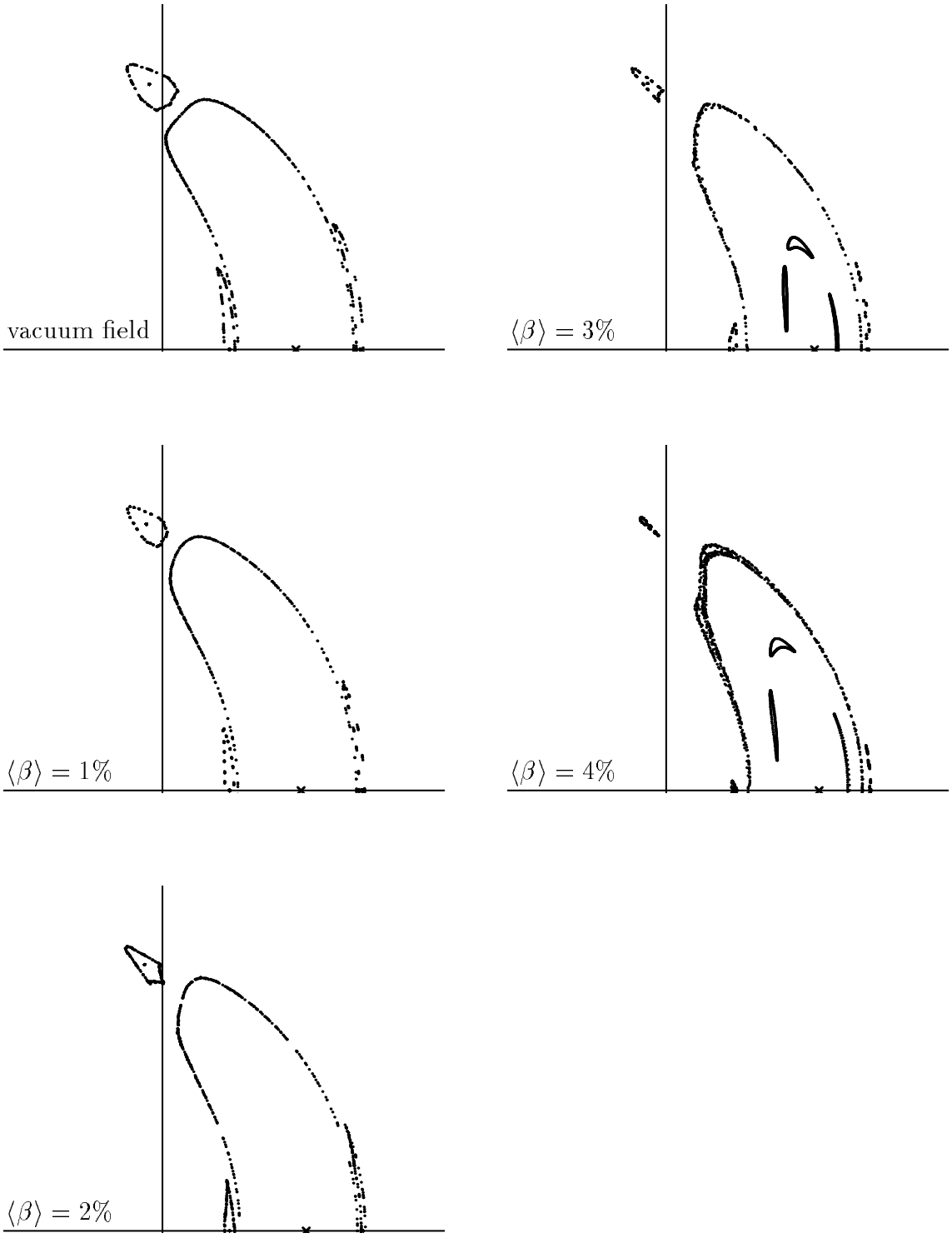

FIG. 7c: Upper halves of Poincaré plots of the high-iota case (case C) for various β-values. At the symmetric bean-shaped cross-section the magnetic axis (cross), the LCMS and the macroscopic island remnants with their O-points are plotted. For $\langle\beta\rangle = 3$ and 4% also the 5/5 islands inside the plasma are shown.

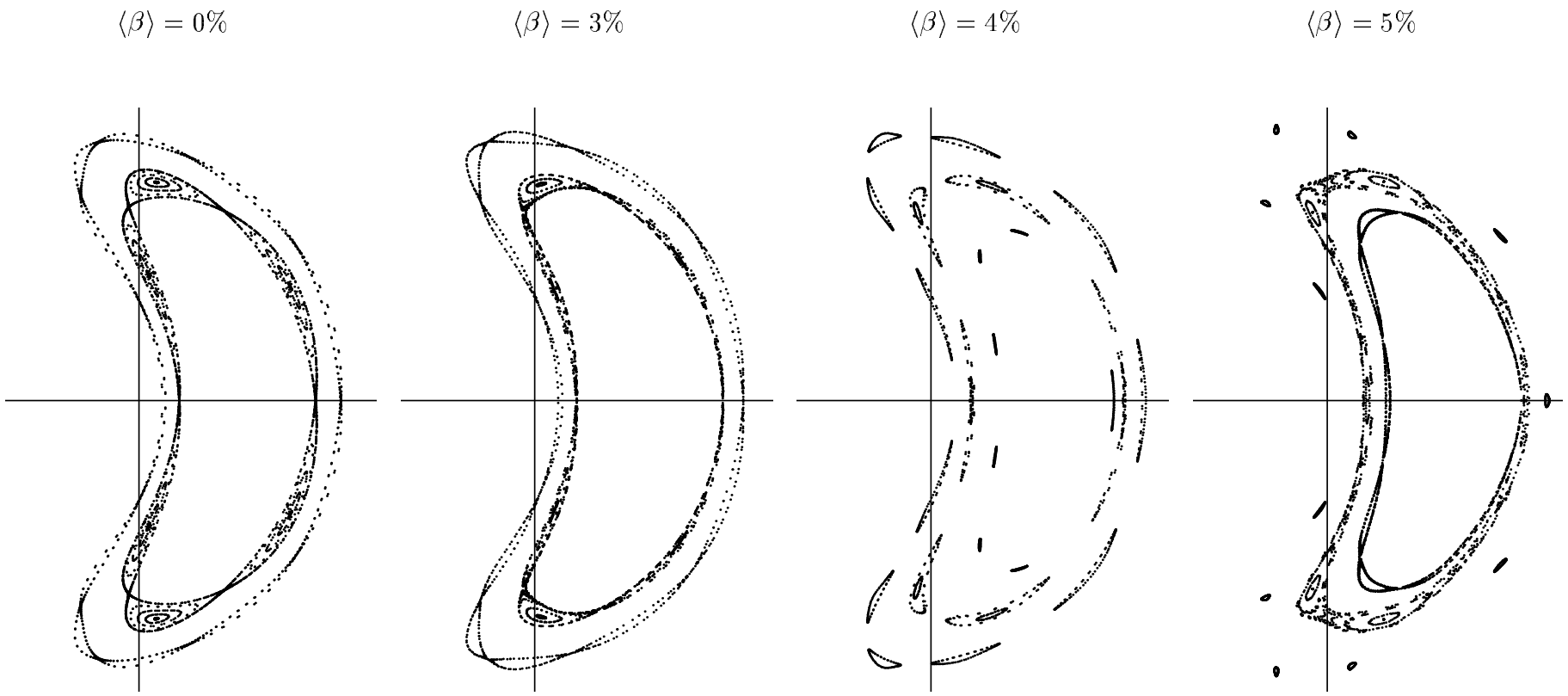

FIG. 8: *Case A: phase shift of the 5/7, 5/6 and 10/11 islands. The islands are plotted for* $\langle\beta\rangle$ *= 0, 3, 4 and 5%.*

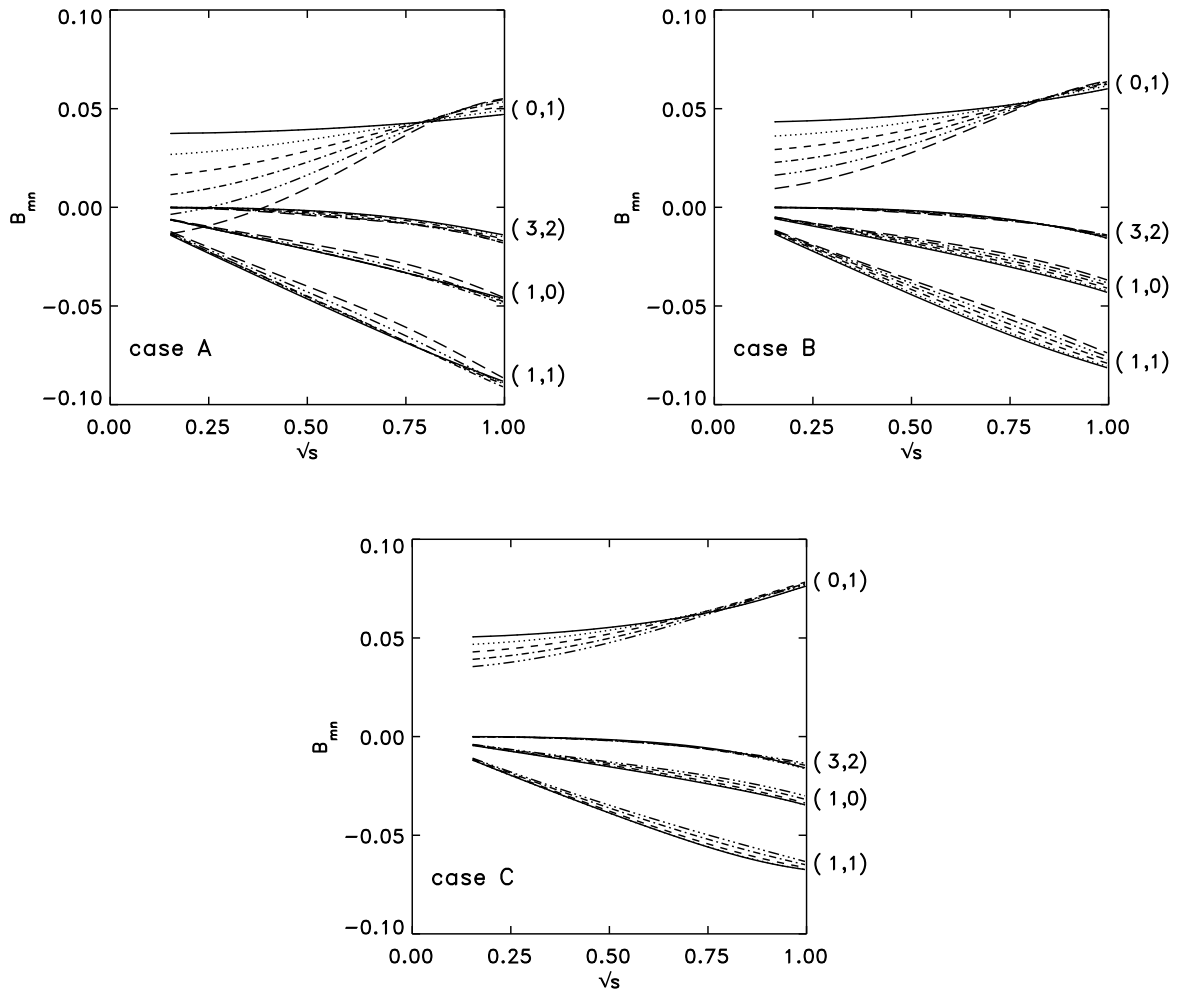

FIG. 9: The $B_{m,n}$s for the cases A, B and C and $\langle\beta\rangle$ = 0% (solid), 1% (dotted), 2% (dashed), 3% (dash dot), 4% (dash dot dot dot) and 5% (long dashes) are plotted versus $\sqrt{s}$ with s = flux label. Fourier coefficients smaller than 0.01 and $B_{0,0}$ are not shown.

Figure 9 shows the dependency of the $B_{m,n}$s on the volume-averaged β-value for the cases A, B and C. There, only the largest Fourier coefficients except for $B_{0,0}$, which shows the largest dependency on β, are plotted. The variation with β decreases with increasing mode number and increasing rotational transform, that is, the Fourier coefficient $B_{0,1}$ of case A shows the largest dependency in Fig. 9. The weak β-dependency of the $B_{m,n}$s (except for $B_{0,0}$, which contains the deepening of the magnetic well) is a consequence of the small change in geometry of the flux-surfaces as β is increased (see Figs 6a,b), which itself is of course due to the small Pfirsch-Schlüter current density of the optimized Wendelstein 7-X stellarator configuration.

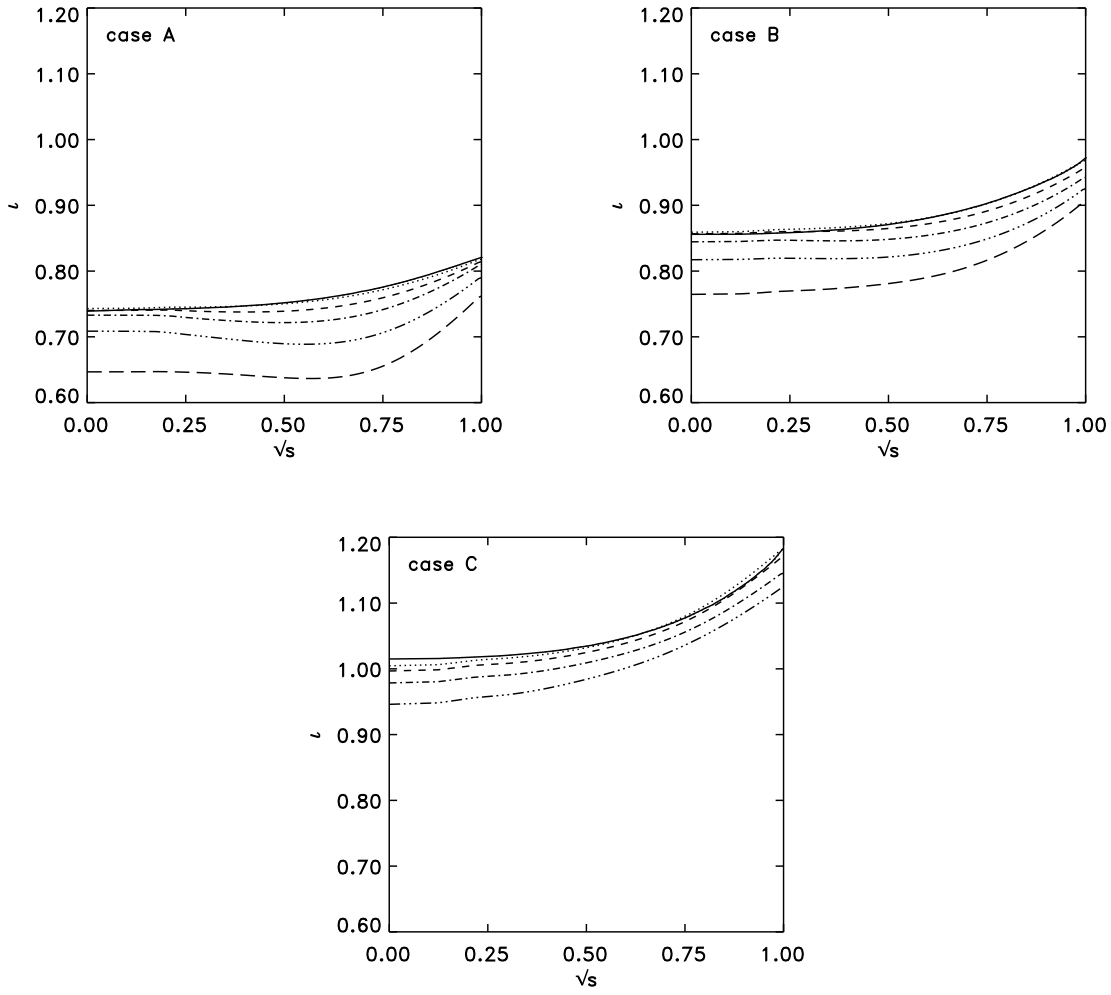

FIG. 10: The rotational transform profiles ι for the cases A, B and C and $\langle\beta\rangle$ = 0% (solid), 1% (dotted), 2% (dashed), 3% (dash dot), 4% (dash dot dot dot) and 5% (long dashes) are plotted versus $\sqrt{s}$ with s = flux label.

In Fig. 10 the rotational transform profiles of the cases A, B, and C are plotted for the considered β-values. Again the low-iota case (case A) shows the largest variation with β.

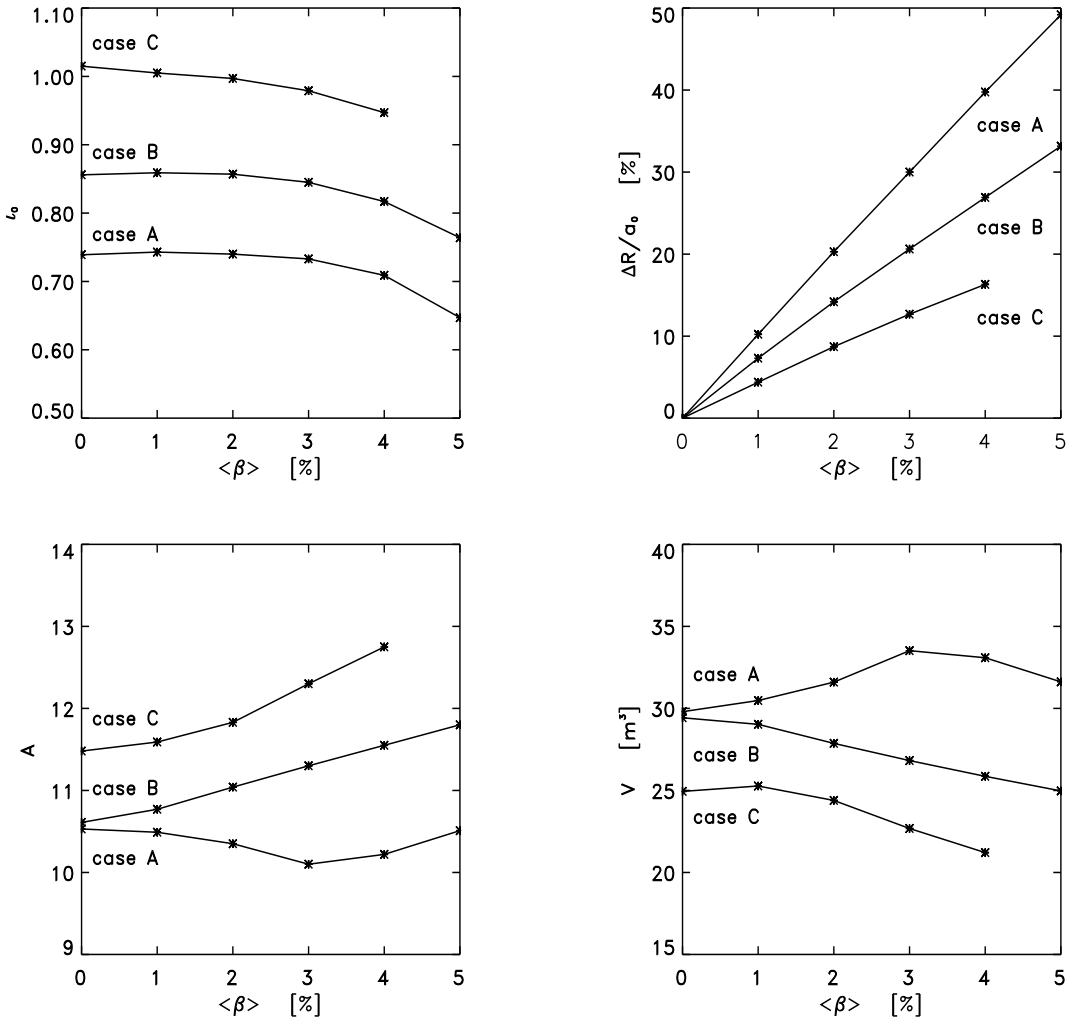

FIG. 11: *Rotational transform ι_0 on the magnetic axis, normalized shift of the magnetic axis $\Delta R/a_0$ (ΔR = mean shift of the magnetic axis, plasma radius: $a_0 = 0.55$ m), aspect ratio A and volume V enclosed by the LCMS versus $\langle\beta\rangle$ for the cases A, B and C.*

The β-dependencies of the rotational transform ι_0 on the magnetic axis, the normalized shift of the magnetic axis $\Delta R/a_0$ (ΔR = mean shift of the magnetic axis, plasma radius: $a_0 = 0.55$ m), the aspect ratio A and the volume V enclosed by the LCMS are summed up in Fig. 11. For case A the aspect ratio A and the plasma volume V as functions of $\langle\beta\rangle$ show a behaviour different from those of case B and case C because of the phase shift of the macroscopic islands.

3.2 MHD stability properties

The MHD stability properties of the finite-β equilibria are studied with respect to the Mercier [17] and resistive interchange [18] criteria by means of the JMC code [14 – 16].

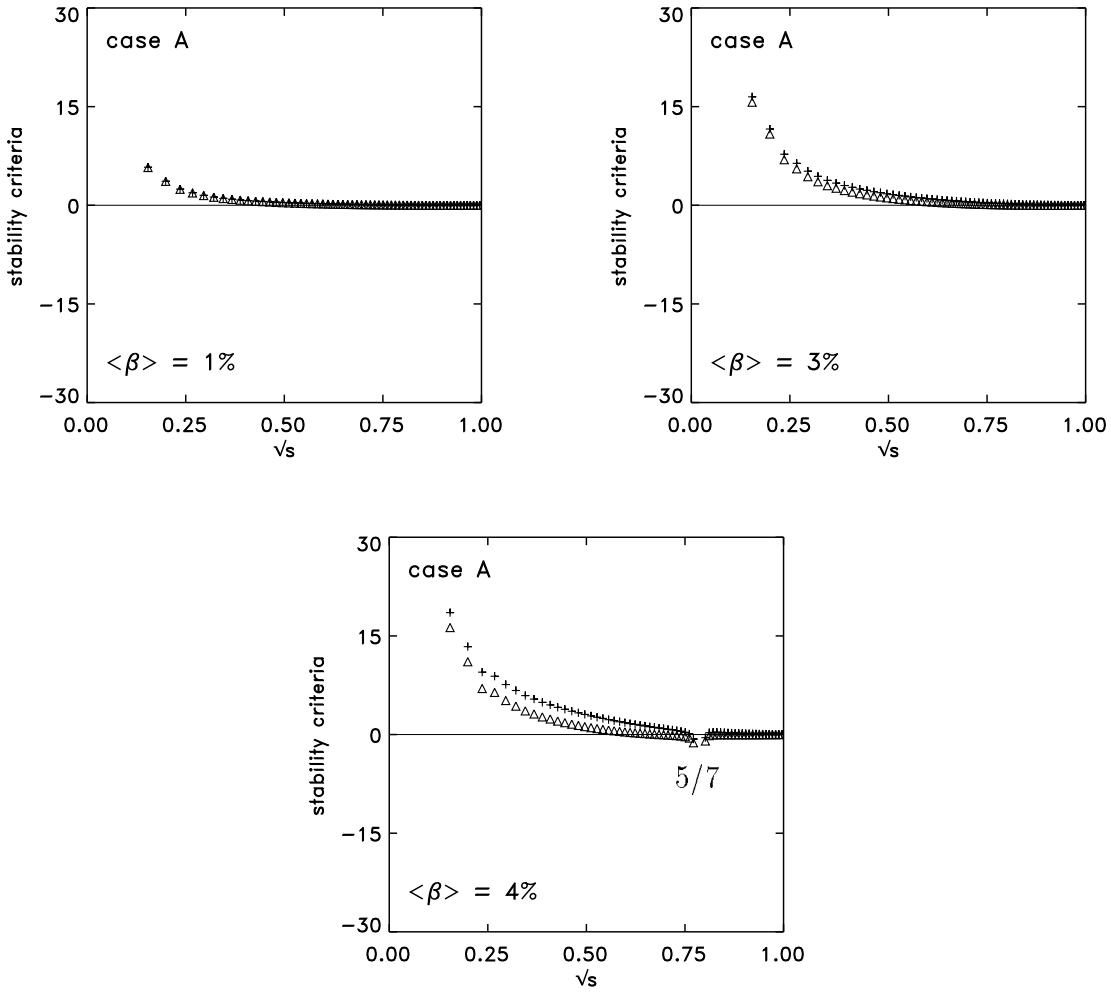

FIG. 12a: Mercier (+) and resistive interchange (Δ) criteria versus $\sqrt{s}$ of case A for $\langle\beta\rangle$ = 1, 3 and 4%.

Figures 12a and 12b show the Mercier (+) and resistive interchange (Δ) criteria of the cases A, B, and C for $\langle\beta\rangle = 1$, 3 and 4%. The cases A, B and C are stable with resepect to these criteria up to $\langle\beta\rangle = 3\%$. For higher β-values formal instability prevails around the 5/7 (case A), 5/6 (case B) and 5/5 (case C) resonances. The formation of these resonances may be suppressed by suitably chosen coil currents [25], and it also depends on the used mass profile (see Section 3.3).

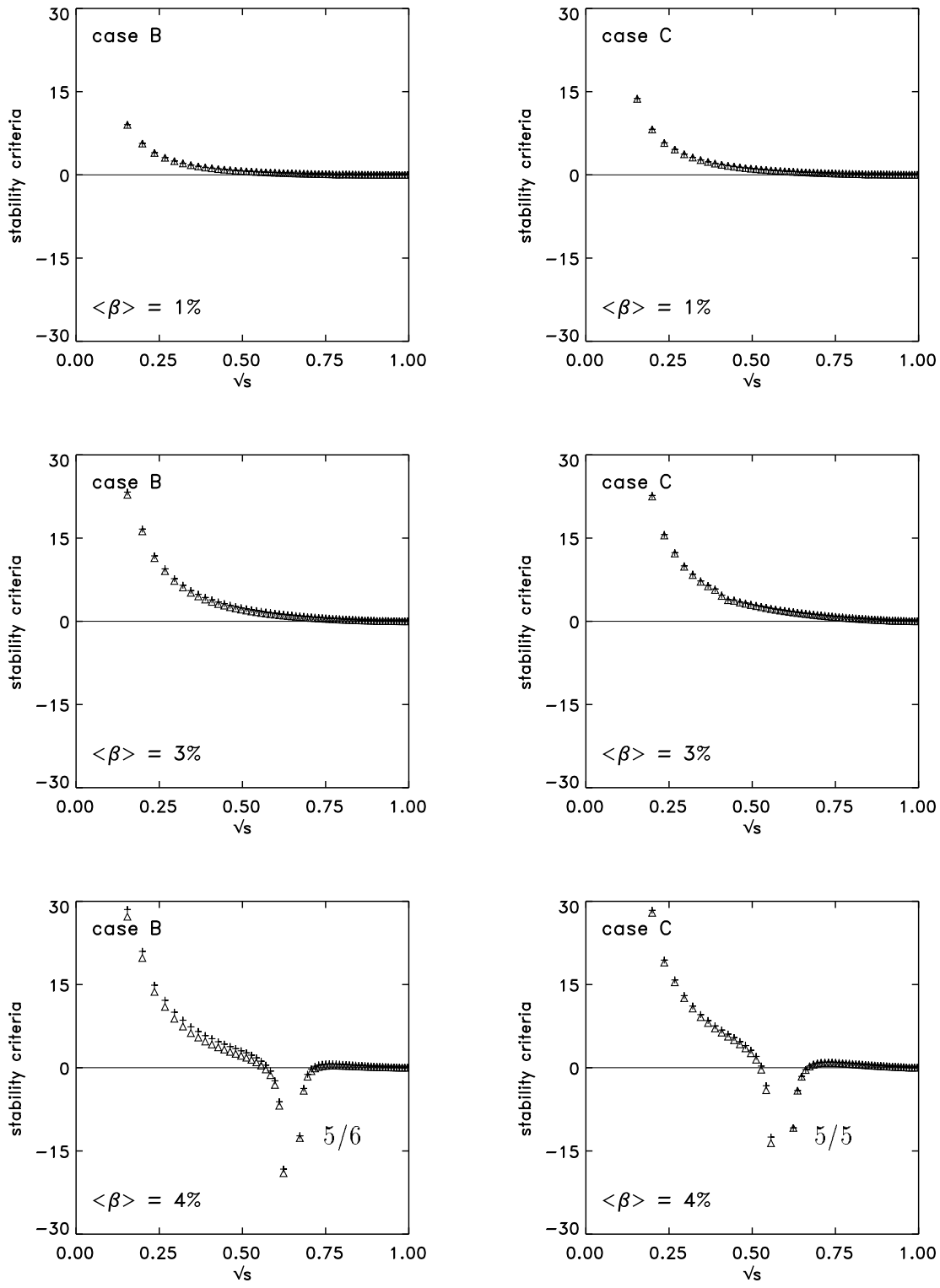

FIG. 12b: Mercier (+) and resistive interchange (Δ) criteria versus $\sqrt{s}$ of the cases B and C for $\langle\beta\rangle$ = 1, 3 and 4%.

3.3 Influence of the mass profile

As already mentioned a mass profile has to be provided as input to the NEMEC code. In this Section equilibria obtained with the Type II mass profile will be compared with those of the Type I profile.

The Type II mass profile leads to a reduction of the maximum beta value at the magnetic axis, that is, for mass profile Type I the maximum beta value is three times larger than the volume-averaged value, while for mass profile Type II the maximum beta value is only 2.4 times lager. With the β-profile also the $B_{m,n}$s, the ι-profile and the shift of the magnetic axis vary.

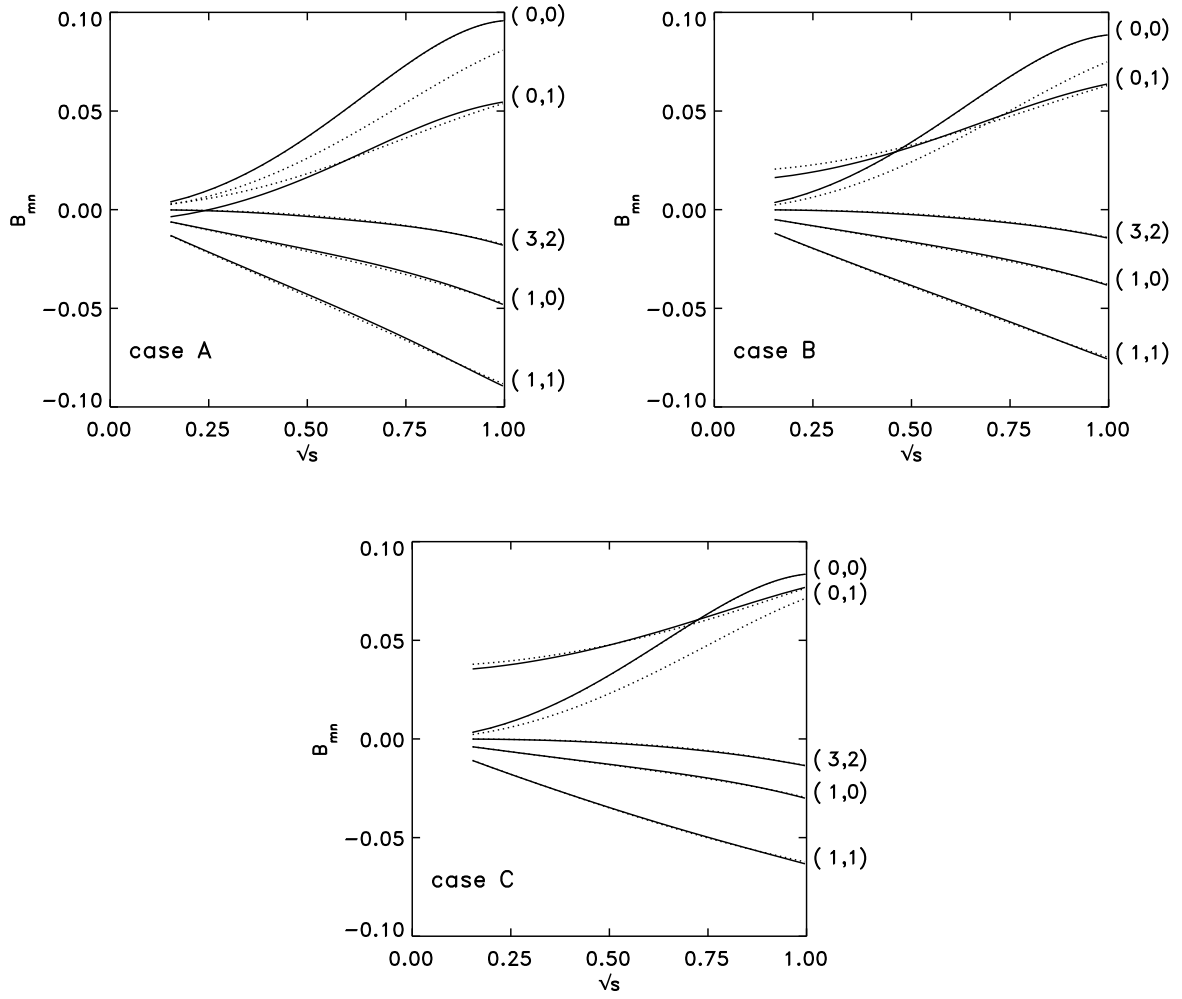

FIG. 13: For the mass profiles Type I (solid) and II (dotted) the $B_{m,n}$s of the cases A, B and C with $\langle\beta\rangle = 4\%$ are plotted versus $\sqrt{s}$ with s = flux label. Fourier coefficients smaller than 0.01 are not shown and $B_{0,0}(s = 0) = 1$ has been subtracted in plotting $B_{0,0}$.

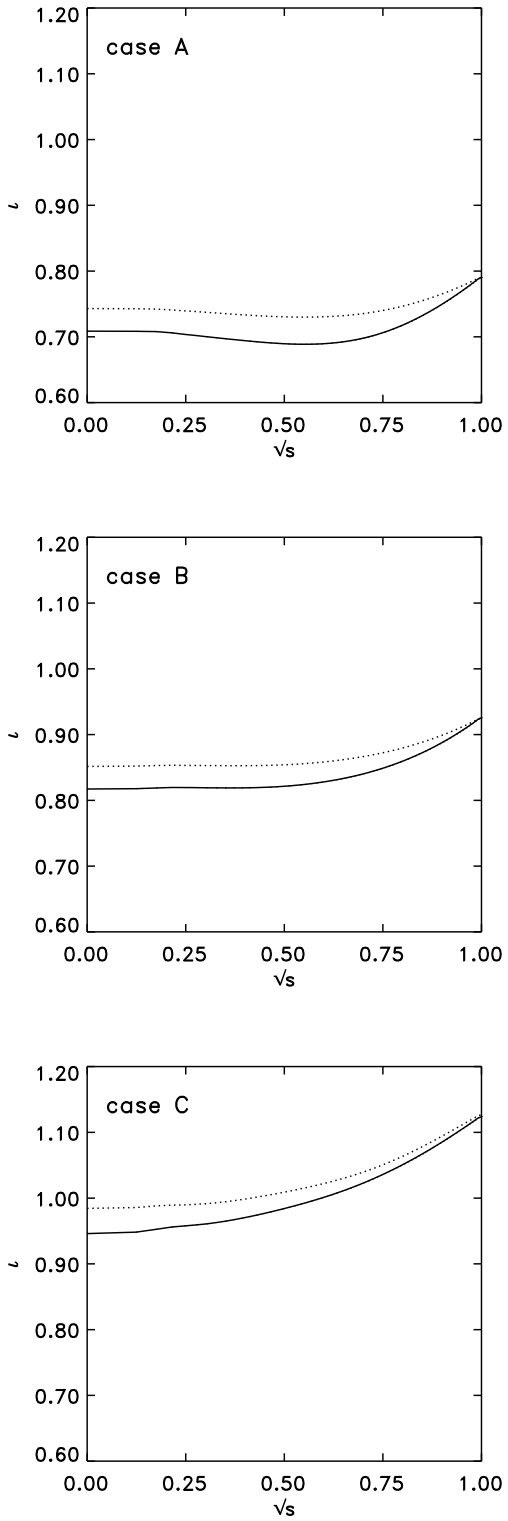

FIG. 14: The rotational transform profiles ι of the cases A, B and C for $\langle\beta\rangle = 4\%$ and the mass profiles Type I (solid line) and Type II (dots).

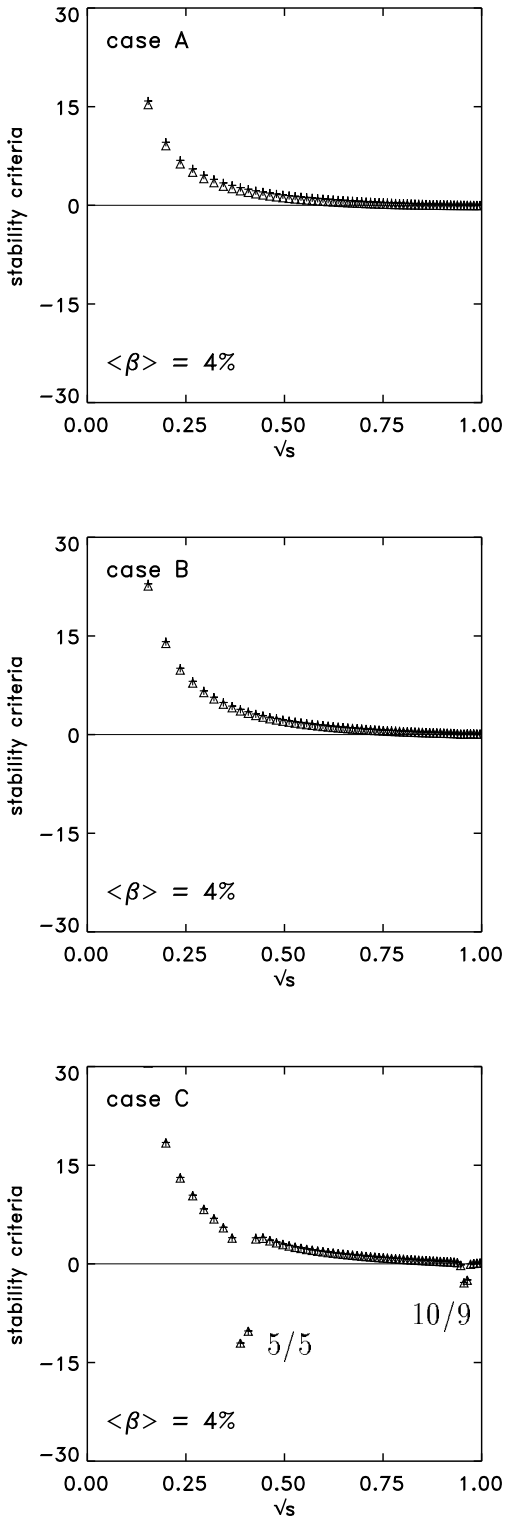

FIG. 15: Mercier (+) and resistive interchange (Δ) criteria versus $\sqrt{s}$ of the cases A, B and C for $\langle\beta\rangle = 4\%$ and mass profile Type II.

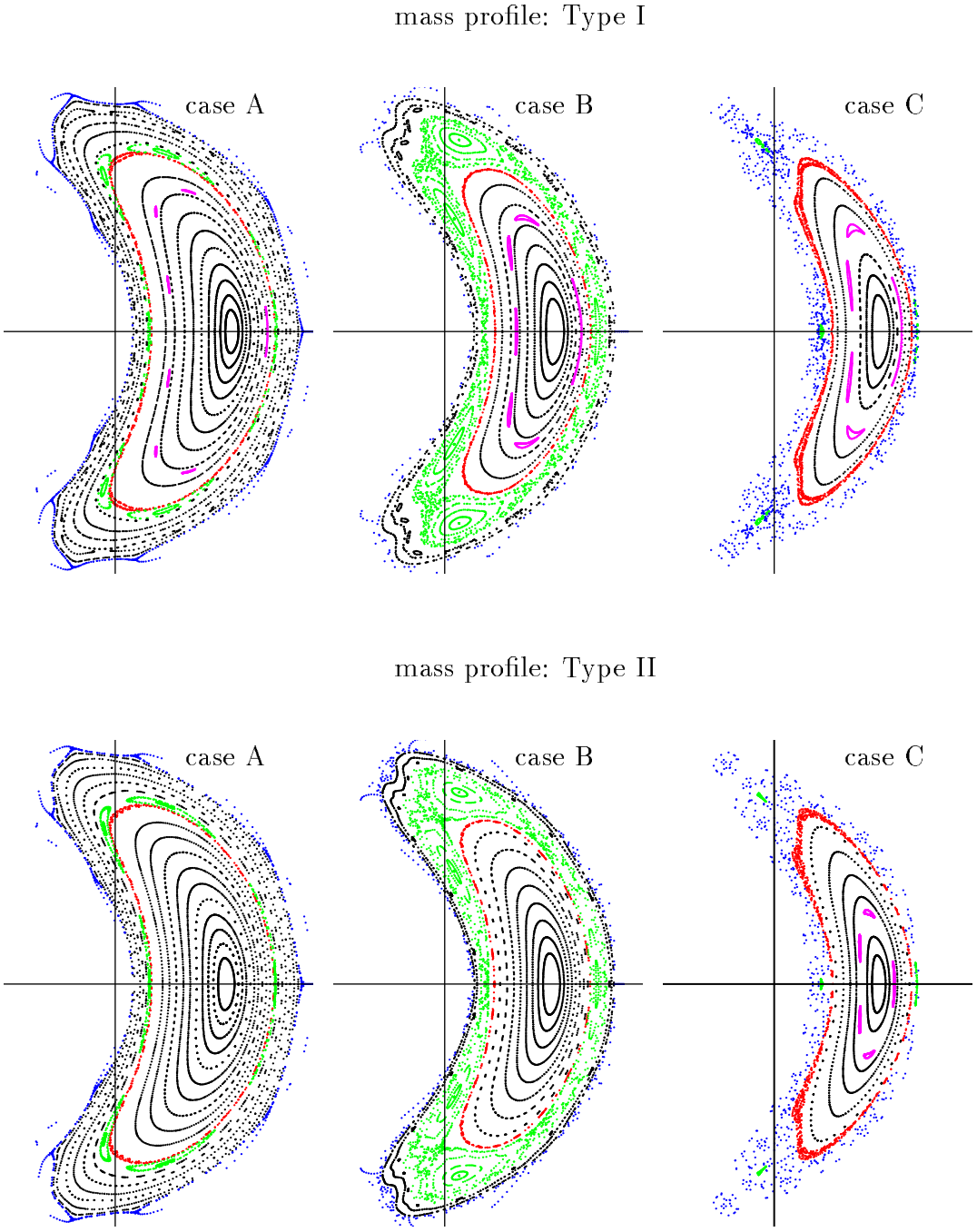

FIG. 16: Poincaré plots of the magnetic fields of the cases A, B and C for the mass profiles Type I and II. At the symmetric bean-shaped cross-section flux surfaces (black dots), macroscopic islands (green dots), the last closed magnetic surface (red dots) and stochastic field lines (blue dots) are plotted. The resonances $\iota = 5/7$ (case A), $\iota = 5/6$ (case B) and $\iota = 5/5$ (case C) are illustrated by pink dots. The volume-averaged β value amounts to 4%.

In Fig. 13 the $B_{m,n}$s of the cases A, B and C with $\langle\beta\rangle = 4\%$ are compared for the two profiles. The Fourier coefficient $B_{0,0}$, which contains the deepening of the magnetic well at finite-β, shows the largest dependency followed by the coefficient $B_{0,1}$ describing the mirror field. The $B_{m,n}$s with higher mode numbers are almost independent of the mass profile.

The lower maximum β-value belonging to mass profile Type II leads to a weaker decrease of the rotational transform with increasing β. This behaviour is shown in Fig. 14. It leads to a formally better stability behaviour with respect to the Mercier and resistive interchange criteria (see Fig. 15), that is, the resonances $\iota = 5/7$ (case A) and $\iota = 5/6$ (case B) do not appear up to $\langle\beta\rangle = 4\%$, and the resonance $\iota = 5/5$ (case C) is smaller and more closely located to the magnetic axis (compare Figs 12a,b and Fig. 15).

The shift of the magnetic axis is also reduced by 25% (case A), 16% (case B) and 15% (case C) using mass profile Type II. Figure 16 shows the Poincaré plots of the bean-shaped cross-sections for the cases A, B and C with $\langle\beta\rangle = 4\%$ obtained with the mass profiles Type I and II. These plots illustrate the reduction of the shift of the magnetic axis and the smaller decrease of the rotational transform (the 5/7 islands (case A) and 5/6 islands (case B) do not appear) by using mass profile Type II. Furthermore, the plots also demonstrate that the edge region is almost independent of the mass profile, that is, the mass profile mostly influences the magnetic field properties inside the LCMS, while the edge region is hardly concerned (at least for the two considered mass profiles).

4. Summary

Magnetic fields have been calculated for finite-β equilibria of up to $\langle\beta\rangle = 5\%$ and edge rotational transform values of $\iota = 5/5$, $5/6$ and $5/4$ using the coil set HS5V10U and two types of mass profiles. Comparisons of the finite-β magnetic fields with the corresponding vacuum fields confirm the properties expected for optimized Helias configurations, namely small outward shift of the plasma column, slight decrease of the rotational transform and almost stationary positions of the X- and O-points of the macroscopic islands. Besides this general behaviour the low-iota, standard and high-iota cases also show some differences. For example, the outward shift of the plasma column increases from the high-iota to the low-iota case. The width of the $5/5$ islands increases with increasing β, while the remnants of the $5/4$ islands become smaller because of the increasing ergodization of the edge region. Further, the width of the $5/6$ islands slightly decreases up to $\langle\beta\rangle = 3\%$, while for $\langle\beta\rangle \geq 4\%$ a phase shift of the islands is observed. The form of the mass profile mostly influences the properties inside the LCMS (e.g. shift of the magnetic axis, rotational transform etc.), while the edge region is hardly concerned.

Acknowledgments

The author is most grateful to J. Nührenberg for many fruitful discussions, and to J. Kisslinger for providing the coil currents.

REFERENCES

[1] GRIEGER, G., BEIDLER, C., HARMEYER, E., HERRNEGGER, F., JUNKER, J., KISSLINGER, J., LOTZ, W., MAASSBERG, H., MERKEL, P., NÜHRENBERG, J., RAU, F., SAPPER, J., SARDEI, E., SCHLÜTER, A., WOBIG, H., in Plasma Physics and Controlled Nuclear Fusion Research (Proc. 13th Int. Conf. Washington 1990) Vol. **3**, IAEA, Vienna (1991) 525.

[2] LOTZ, W., NÜHRENBERG, J., SCHWAB, C., in Plasma Physics and Controlled Nuclear Fusion Research (Proc. 13th Int. Conf. Washington 1990) Vol. **2**, IAEA, Vienna (1991) 603.

[3] Wendelstein Project Group, Euratom-IPP Association, Wendelstein 7-X, Phase II, Application for Preferential Support, 1994.

[4] GREUNER, H., BITTER, W., KERL, F., KISSLINGER, J., RENNER, H., in Fusion Technology 1994 (Proc. of 18th Symp. on Fusion Technology, Karlsruhe 1994) Vol **1**, ELSEVIER SCIENCE B.V., Amsterdam (1995) 323.

[5] KISSLINGER, J., BEIDLER, C.D., HARMEYER, E., RAU, F., RENNER, H., WOBIG, H., Proc. 21th EPS Conf. on Contr. Fusion and Plasma Physics, Montpellier 1994, ECA, Vol **18B**, Part I, 368.

[6] KISSLINGER, J., BEIDLER, C.D., HARMEYER, E., RAU, F., RENNER, H., WOBIG, H., Proc. 22th EPS Conf. on Contr. Fusion and Plasma Physics, Bournemouth 1995, ECA, Vol **19C**, Part III, 149.

[7] KISSLINGER, J., BEIDLER, C.D., HARMEYER, E., RAU, F., RENNER, H., WOBIG, H., in: Proc. 10th Int. Conf. on Stellarators, IEA Techn. Comm. Meeting Madrid 1995, Eds. Ascasibar, E., Aranda, D., EUR-CIEMAT 30, CIEMAT, Madrid 1995, 290.

[8] STRUMBERGER, E., Nuclear Fusion **36** (1996) 891.

[9] HIRSHMAN, S.P., MEIER, H.K., Phys. Fluids **28** (1985) 1387.

[10] HIRSHMAN, S.P., Lee, D.K., Comput. Phys. Commun. **39** (1986) 161.

[11] HIRSHMAN, S.P., van RIJ, W.I., MERKEL, P., Comput. Phys. Comm. **43** (1986) 143.

[12] MERKEL, P., J. Comput. Phys. **66** (1986) 83.

[13] STRUMBERGER, E., Nuclear Fusion **37** (1997) 19.

[14] NÜHRENBERG, J., ZILLE, R., Phys. Lett. A **114** (1986) 129.

[15] NÜHRENBERG, J., ZILLE, R., Phys. Lett. A **129** (1988) 113.

[16] NÜHRENBERG, J., ZILLE, R., in Proc. Workshop on Theory of Fusion Plasma, Varenna 1987, Eds. A. Bondesin, E. Sindoni, F. Troyon, 1988, EUR 11336 EN, 3.

[17] MERCIER, C., in Plasma Physics and Contr. Nucl. Fusion Res. 1961, Nucl. Fusion 1962 Suppl. 2, IAEA, Vienna (1962) 801.

[18] GLASSER, A.H., GREEN, J.M., JOHNSON, J.L., Phys. Fluids **18** (1975) 875.

[19] BOOZER, A., Phys. Fluids **23** (1980) 904.

[20] HIRSHMAN, S.P., WHITSON, J.C., Phys. Fluids **26** (1983) 3553.

[21] STRUMBERGER, E., Contr. to Plasma Phys., in print.

[22] REIMAN, A.H., GREENSIDE, H.S., Comput. Phys. Commun. **43** (1986) 157.

[23] REIMAN, A.H., GREENSIDE, H.S., J. Comput. Phys. **87** (1990) 349.

[24] ARNDT, S., MONTICELLO, D.A., REIMAN, A.H., Proc. 21th EPS Conf. on Contr. Fusion and Plasma Physics, Berchtesgaden 1997, EPS, Vol **21A**, Part IV, 1661.

[25] STRUMBERGER, E., ZILLE, R., et al., Laboratory Report IPP 2/333, Garching 1996.